AIAA JOURNAL
Vol. 47, No. 6, June 2009

# Three-Dimensional Simulation of the Electric Field and Magnetohydrodynamic Power Generation During Reentry

Tian Wan* and Graham V. Candler†
*University of Minnesota, Minneapolis, Minnesota 55455*
and
Sergey O. Macheret‡ and Mikhail N. Shneider§
*Princeton University, Princeton, New Jersey 08540*

DOI: 10.2514/1.32006

**A numerical tool is developed to help design magnetohydrodynamics power-generation panels to be used onboard a reentry vehicle. The tool consists of two parts: a magnetohydrodynamics flow solver and a Poisson solver. The magnetohydrodynamics flow solver deals with the two-dimensional Navier–Stokes equations extended to incorporate magnetohydrodynamics effects and chemical reactions. The Poisson equation for the electric potential is discretized with a 19-point stencil in three-dimensional space. The Poisson solver is tested with three cases, and all the results reproduce the analytical solutions and those from the literature. Then it is used to compute the electric field, current-density distributions, and total power generation around a reentry vehicle with onboard electrodes. We compare the results with the previous two-dimensional simulation results. Several three-dimensional plots of the current stream traces are presented, and from the plots the current is categorized into five types. The net current through each electrode surface and the corresponding power extraction are computed. At the present stage, the magnetohydrodynamics Poisson solver is uncoupled from the flow solver.**

## Nomenclature

| | | |
|---|---|---|
| $a, b, c$ | = | coefficients in the approximate factorization method |
| $\mathbf{B}$ | = | vector of magnetic induction, T |
| $D$ | = | diffusion coefficient, $m^2 \cdot s^{-1}$ |
| $E$ | = | energy, $J \cdot m^{-3}$ |
| $\mathbf{E}$ | = | vector of the electric field, $V \cdot m^{-1}$ |
| $e$ | = | specific energy, $J \cdot kg^{-1}$ |
| $\mathbf{j}$ | = | vector of the electric current density, $A \cdot m^{-2}$ |
| $M$ | = | mass of heavy particle, kg |
| $m$ | = | mass, kg |
| $\hat{n}$ | = | surface unit normal vector |
| $n_d$ | = | number of diatomic molecule |
| $n_{\max}$ | = | maximum number of iterations |
| $p$ | = | pressure, Pa |
| $Q_{T\text{-}V}$ | = | translational-vibrational energy transfer rate, $J \cdot m^{-3} \cdot s^{-1}$ |
| $q$ | = | heat flux, $J \cdot m^{-2} \cdot s^{-1}$ |
| $R$ | = | residual |
| $S$ | = | surface area, $m^2$ |
| $\mathbf{S}$ | = | surface normal vector, $m^2$ |
| $Sr$ | = | source term due to interaction of flow and magnetic field |
| $t$ | = | time, s |
| $\mathbf{u}$ | = | velocity, $m \cdot s^{-1}$ |
| $\mathbf{v}$ | = | diffusion velocity, $m \cdot s^{-1}$ |
| $\alpha_p$ | = | relaxation parameter |
| $\nu$ | = | collision frequency, $s^{-1}$ |
| $\xi, \eta, \zeta$ | = | coordinates in computational space |
| $\rho$ | = | density, $kg \cdot m^{-3}$ |
| $\sigma$ | = | electrical conductivity, $mho \cdot m^{-1}$ |
| $\hat{\sigma}$ | = | effective conductivity, $mho \cdot m^{-1}$ |
| $\tilde{\sigma}$ | = | conductivity tensor, $mho \cdot m^{-1}$ |
| $\tilde{\tau}$ | = | shear-stress tensor, $N \cdot m^{-2}$ |
| $\phi$ | = | scalar potential, V |
| $\Omega_e$ | = | Hall parameter |
| $\hat{\Omega}_e$ | = | effective Hall parameter |
| $\Omega_i$ | = | ion Hall parameter |
| $\omega$ | = | generation rate, $kg \cdot m^{-3} \cdot s^{-1}$ |
| $\omega_v$ | = | source term for vibrational energy, $J \cdot m^{-3} \cdot s^{-1}$ |

*Subscripts*

| | | |
|---|---|---|
| $e, i, n$ | = | electron, ion, and neutral particles |
| $i, j, k$ | = | $x$, $y$, and $z$ components |
| $s$ | = | species $s$ |
| $v$ | = | vibration |
| $x, y, z$ | = | $x$, $y$, and $z$ directions |

*Superscripts*

| | | |
|---|---|---|
| $(0), (n)$ | = | number of intermediate $\Delta\phi$ |

Received 7 May 2007; revision received 14 July 2008; accepted for publication 17 July 2008. 

*Graduate Research Assistant, Aerospace Engineering and Mechanics Department; wan@aem.umn.edu. Student Member AIAA.

†Professor, Aerospace Engineering and Mechanics Department. Fellow AIAA.

‡Senior Research Scientist, Department of Mechanical and Aerospace Engineering; currently Lockheed Martin Aeronautics Company, Advanced Development Programs, 1011 Lockheed Way, Palmdale, CA 93599-0160. Associate Fellow AIAA.

§Research Staff Member, Department of Mechanical and Aerospace Engineering. Senior Member AIAA.

## I. Introduction

WHEN ionized flow passes through a magnetic field, the electrons drift and a current forms that can be extracted by electrodes. There are several possible applications for this technology. For example, if power can be extracted from the high-speed flow, control surfaces could be actuated without the requirements for additional battery power. In recent work [1–3], computational fluid dynamics was used to explore the possibility of magnetohydrodynamics (MHD) power generation during planetary reentry. The high-speed air between the bow shock and boundary layer has

high temperature during reentry, which makes it an appropriate working flow for MHD generators. A small amount of seeding can provide the necessary number of high-mobility electrons. The previous results showed that megawatt per square meter power levels can be generated with a small amount of potassium seed (∼1% by mass) and modest values of magnetic field (0.1–0.2 T). In the previous work, both the flowfield and electromagnetic field are assumed to be two-dimensional.

In the present work, we solve for the three-dimensional electric field and current density, and the flowfield is assumed to be two-dimensional. The diagram of the problem is shown in Fig. 1. The vehicle has the shape of a blunt wedge with a 25 deg angle and a nose radius of 0.1 m, with alternating anodes and cathodes placed on top. The electrodes have the size of 7 cm height and 2.5 m length, and they are placed with a 1 m separation. The 7 cm height is set based on the previous two-dimensional analysis. The electrode thickness (shown in Fig. 1a) has the value of 9 mm unless stated otherwise. We currently assume that the potassium seed is injected upstream from the vehicle. Figure 1b shows that the seeding beam is injected toward the vehicle nose and is of 3 cm width above the stagnation line. All the computations in the present paper are with 1%-by-mass potassium seeding by assumption. Practically, sodium-potassium (NaK) vapor could be injected through the vehicle surface, but the details of the seeding injection system are not addressed in the present work.

The hypersonic flow past a blunt reentry vehicle is simulated with our MHD flow solver [1–3]. The flowfield is described by the Navier–Stokes equations extended to include nonequilibrium thermochemistry. A 13-species chemistry model, including finite rate potassium ionization and recombination, is used to simulate the air reactions at high temperature. The two-dimensional flowfield simulation is performed on the center plane between the electrodes. Then the calculated results are exported, by assuming uniform flow in the third direction, to the Poisson solver, which computes the three-dimensional electric field and current distributions, as well as the corresponding power extraction. The Poisson equation arises

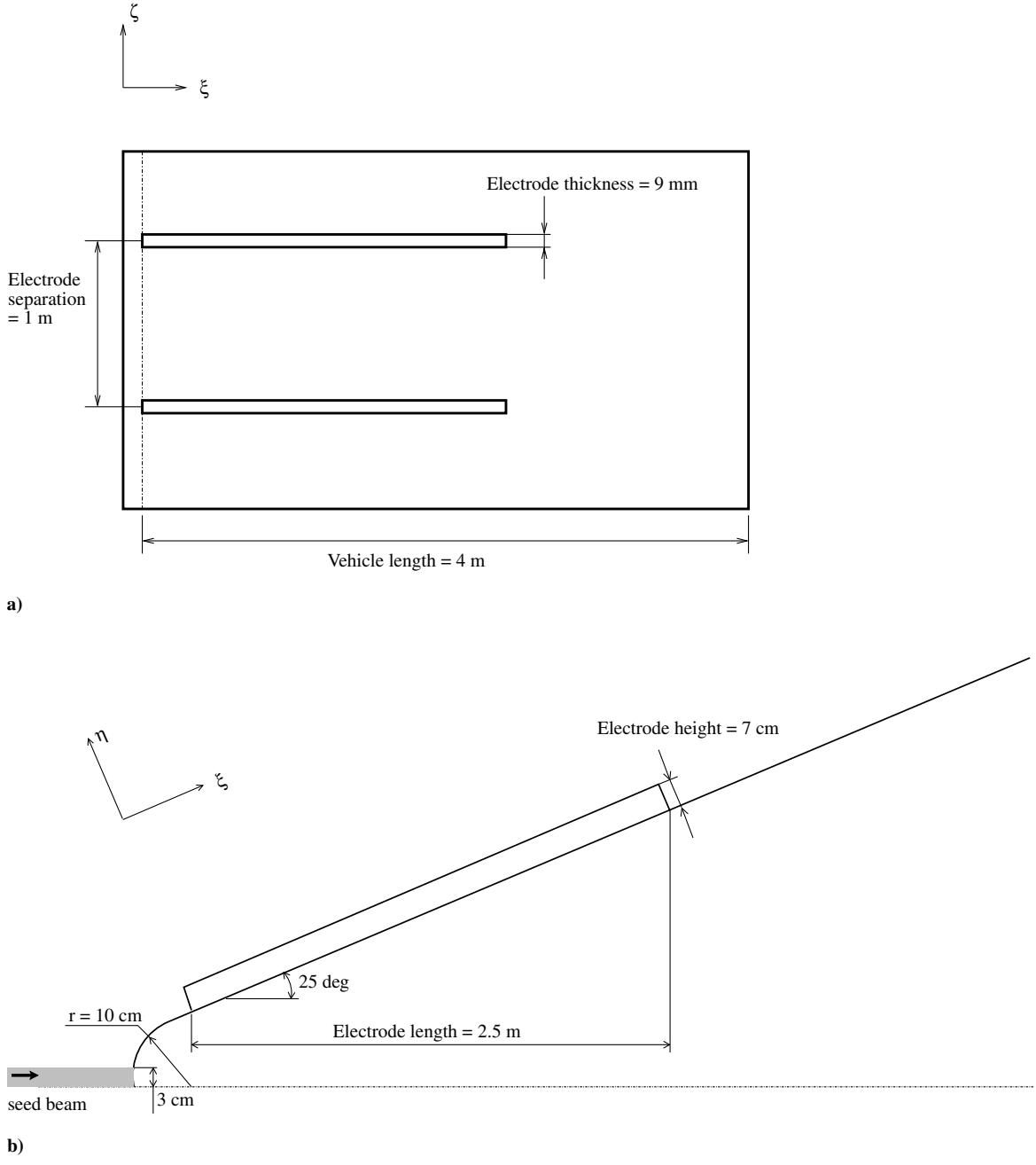


**Fig. 1 Diagrams of the MHD reentry vehicle setup.**

from the current continuity equation [4]. In [4] this equation is discretized with a high-order Padé-type scheme (see also [5]). In this paper, we solve the equation with a 19-point-stencil finite volume method. Although a Padé-type scheme has high-order accuracy in one dimension locally, our 19-point stencil takes into account the surrounding grid points in all three dimensions. The Poisson solver is tested with three cases taken from [4], and the results are presented.

The 2-D flowfield calculation neglects the influence of the electrodes on the flow, as well as the three-dimensional aspects of the current distribution, which result in a three-dimensional Joule heating distribution. With the present continuous electrodes, shocks and boundary layer will be generated by the electrodes. Hence, gas composition and electrical conductivity close to the electrodes can only be computed with a three-dimensional code. However, such a full simulation is beyond the scope of this paper, and we expect that most of the difference will be in the regions near the electrodes and vehicle surface, and not in the power extraction. We will conduct three-dimensional flowfield calculation and use electrodes of different shapes (flush electrodes, for example) in future work.

In this paper, the governing equations and assumptions of the MHD flow solver are presented, followed by a detailed description of the Poisson equation and its solution strategy and validation. Then the MHD flow solver and Poisson solver are used to compute MHD power generation during reentry, and the results are compared with previous two-dimensional calculations.

## II. Governing Equations of the MHD Flow Solver

Our numerical simulations use the data-parallel line-relaxation (DPLR) [6] method to solve the Navier–Stokes equations coupled with nonequilibrium thermochemistry. The DPLR method is a parallel version of the original Gauss–Seidel line-relaxation method [7] that takes advantage of the flow physics and solves the linearized equations exactly in the direction normal to the wall, which is the direction in which the solution has strong physical coupling in high-Reynolds-number flows, whereas in the tangential direction to the wall, point relaxation is applied. The code has been modified to incorporate MHD effects, assuming a low magnetic Reynolds number. We use an 11-species ($N_2$, $O_2$, NO, N, O, $N_2^+$, $O_2^+$, $NO^+$, $O^+$, $N^+$, and $e^-$) air chemistry model. Including the 2 seed species (potassium atom and potassium ion), a total of 13 equations are solved for mass conservation, which take the form

$$\frac{\partial \rho_s}{\partial t} + \nabla \cdot (\rho_s \mathbf{u}) + \nabla \cdot (\rho_s \mathbf{v}_s) = \omega_s \tag{1}$$

The momentum equation is expressed as

$$\frac{\partial (\rho \mathbf{u})}{\partial t} + \nabla \cdot (\rho \mathbf{u} \otimes \mathbf{u}) + \nabla p + \nabla \cdot \tilde{\tau} = \mathbf{j} \times \mathbf{B} \tag{2}$$

where the Lorentz force appears on the right-hand side. For this work, the mass diffusion is based on Fick's Law, and a single diffusion coefficient is used for all neutral species by assuming a constant Lewis number. For the ionic species, the ambipolar diffusion coefficient is used, and within the context of the ambipolar diffusion approximation, the effective diffusion coefficient of electrons is obtained by equating the diffusion velocity of electrons with that of ions.

We can assume vibrational-electronic-electron equilibrium in the boundary layer in which gas temperature and pressure are around 4000 K and 0.1 atm and the strength of the electric field is modest. In the boundary layer behind the shock, the pressure is very high and hence the vibrational-electron energy transfer rate is high. In the present work, the electronic energy does not go into the vibrational energy pool; instead, we assume that the heavy particles are either in their neutral state or ionized. Then the energy contained in these modes is described by a vibrational-electronic-electron temperature $T_{ve}$. The vibrational-electronic-electron energy conservation equation is given by

$$\frac{\partial E_v}{\partial t} + \nabla \cdot (E_v \mathbf{u}) + \nabla \cdot \mathbf{q}_v + \nabla \cdot \sum_{s=1}^{n_d} \mathbf{v}_s E_{v,s} = w_v + (\mathbf{j} \cdot \mathbf{j})/\sigma \tag{3}$$

where

$$w_v = Q_{T\text{-}V} + \sum_{s=1}^{n_d} w_s e_{vs}$$

is the source term for vibrational energy, and $Q_{T\text{-}V}$ is the translational-vibrational energy transfer rate, which can be found in [7]. The second term on the right-hand side is the Joule heating term. Joule heating heats up electrons and, as a result, the energy transfer rate between electrons and heavy particles increases. We assume that the entire Joule heating goes into the vibrational-electronic mode, whereas, in principle, only a portion does. However, in our case, the contribution of the Joule heating to the overall vibrational energy balance is much smaller than that of the $V$-$T$ term; hence, the assumption does not affect the results in all the cases computed.

The last conservation equation is the total energy equation given by

$$\frac{\partial E}{\partial t} + \nabla \cdot [(E + p)\mathbf{u}] + \nabla \cdot (\mathbf{q} + \mathbf{q}_v) + \nabla \cdot (\mathbf{u} \cdot \tilde{\tau}) + \nabla \cdot \sum_{s=1}^{n_s} \mathbf{v}_s \rho_s h_s = \mathbf{j} \cdot \mathbf{E} \tag{4}$$

where the term on the right-hand side is the power extracted from the flow.

## III. Poisson Equation for Electric Potential

The Poisson equation can be derived using the following three equations:

Continuity:

$$\nabla \cdot \mathbf{j} = 0 \tag{5}$$

Ohm:

$$\mathbf{j} = \tilde{\tilde{\sigma}} \cdot (\mathbf{E} + \mathbf{u} \times \mathbf{B}) \tag{6}$$

Faraday:

$$\nabla \times \mathbf{E} = -\frac{\partial \mathbf{B}}{\partial t} \tag{7}$$

Equation (5) is the steady-state form of the current continuity equation. Equation (6) is the generalized Ohm's law [8], in which the conductivity $\tilde{\tilde{\sigma}}$ is a tensor, for which the expressions are taken from [4]

$$\tilde{\tilde{\sigma}} = \frac{\sigma}{D} \begin{bmatrix} \sigma_{11} & \sigma_{12} & \sigma_{13} \\ \sigma_{21} & \sigma_{22} & \sigma_{23} \\ \sigma_{31} & \sigma_{32} & \sigma_{33} \end{bmatrix} \tag{8}$$

where $D$ and the $\sigma_{ij}$ are

$$D = (1 + \alpha\sigma\mathbf{B}^2)^2 + (\beta\sigma\mathbf{B})^2 \tag{9}$$

$$\sigma_{ij} = (1 + \sigma\alpha\mathbf{B}^2)(\delta_{ij} + \sigma\alpha B_i B_j) + \beta^2\sigma^2 B_i B_j - \sigma\beta\epsilon_{ijk}B_k \quad i, j, k = 1, 2, 3 \tag{10}$$

In the preceding expressions, $\sigma$ is the electron conductivity that is computed with the formulas from [1], and $\alpha$ and $\beta$ are related to the electron and ion Hall parameters, $\Omega_e$ and $\Omega_i$, as follows:

$$\alpha = \frac{\Omega_e \Omega_i}{\sigma \mathbf{B}^2}, \qquad \beta = \frac{\Omega_e}{\sigma |\mathbf{B}|} \tag{11}$$

and

$$\Omega_e = \frac{e|\mathbf{B}|}{m_e(\nu_{en} + \nu_{ei})}, \qquad \Omega_i = \frac{e|\mathbf{B}|}{M\nu_{in}} \tag{12}$$

For our case, we assume that there is only low-frequency variation of magnetic induction; hence, the electric field induced by the change of

magnetic induction is negligible. Then, from the definition of the electrostatic field and scalar potential, Eq. (7) can be simplified as

$$\nabla \times \mathbf{E} = 0, \qquad \mathbf{E} = -\nabla\phi \tag{13}$$

The integrated form of the current continuity equation over an arbitrary volume $V$ is

$$\int_V \nabla \cdot \mathbf{j} \mathrm{d}V = 0 \tag{14}$$

By use of Gauss's theorem, we can rewrite it as

$$\int_S \mathbf{j} \cdot \mathrm{d}\mathbf{S} = 0 \tag{15}$$

The discretized form is

$$(\mathbf{j}\cdot\mathbf{S})_{i+1/2} + (\mathbf{j}\cdot\mathbf{S})_{i-1/2} + (\mathbf{j}\cdot\mathbf{S})_{j+1/2} + (\mathbf{j}\cdot\mathbf{S})_{j-1/2} + (\mathbf{j}\cdot\mathbf{S})_{k+1/2} + (\mathbf{j}\cdot\mathbf{S})_{k-1/2} = 0 \tag{16}$$

With Eqs. (6) and (13), we have the general form of the surface current density as

$$\mathbf{j}\cdot\mathbf{S} = (\tilde{\tilde{\sigma}}\cdot(-\nabla\phi + \mathbf{u}\times\mathbf{B}))\cdot\mathbf{S} \tag{17}$$

After substituting the form of $\tilde{\tilde{\sigma}}$ and collecting terms of derivatives of $\phi$, we obtain the following general form of the surface current density:

$$\mathbf{j}\cdot\mathbf{S} = -\bar{\xi}\frac{\partial\phi}{\partial\xi} - \bar{\eta}\frac{\partial\phi}{\partial\eta} - \bar{\zeta}\frac{\partial\phi}{\partial\zeta} + Sr \tag{18}$$

where

$$\bar{\xi} = \hat{\sigma}S(C_1\xi_x + C_2\xi_y + C_3\xi_z) \tag{19}$$

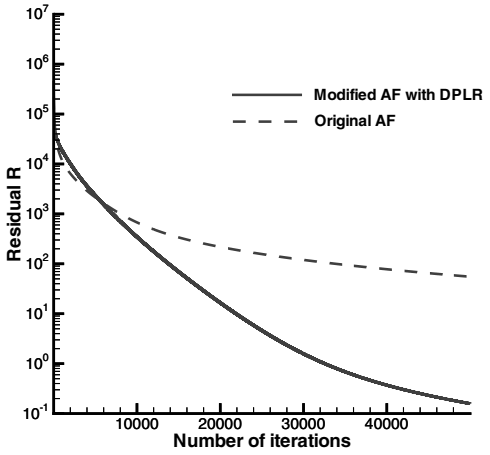


**Fig. 2 Convergence history of the original AF and modified AF with DPLR applied to the MHD power-generation case.**

$$\bar{\eta} = \hat{\sigma}S(C_1\eta_x + C_2\eta_y + C_3\eta_z) \tag{20}$$

$$\bar{\zeta} = \hat{\sigma}S(C_1\zeta_x + C_2\zeta_y + C_3\zeta_z) \tag{21}$$

$$Sr = \hat{\sigma}S\left((\mathbf{u}\times\mathbf{B})\cdot\hat{n} + |\mathbf{B}|\tilde{\Omega}_e\mathbf{u}\cdot\hat{n} - \frac{\mathbf{u}\cdot\mathbf{B}}{|\mathbf{B}|}\tilde{\Omega}_e\mathbf{B}\cdot\hat{n}\right) \tag{22}$$

where $\hat{n}$ is the surface unit normal vector; the coefficients $C_1$, $C_2$, and $C_3$ are given by

$$C_i = n_i - \frac{\tilde{\Omega}_e}{|\mathbf{B}|}\epsilon_{ijk}B_j n_k + \mathbf{B}\cdot\hat{n}B_i g, \qquad i = 1,2,3 \tag{23}$$

and $\hat{\sigma}$ is the effective conductivity, which is the electron conductivity corrected for the Hall effect and ion slip, given by

$$\hat{\sigma} = \frac{\sigma}{(1+\tilde{\Omega}_e^2)(1+\Omega_e\Omega_i)} \tag{24}$$

and

$$\tilde{\Omega}_e = \frac{\Omega_e}{1+\Omega_e\Omega_i} \tag{25}$$

and $g$ is given by

$$g = \frac{\tilde{\Omega}_e}{|\mathbf{B}|^2}(\Omega_e + \Omega_i + \Omega_e\Omega_i^2) \tag{26}$$

Equation (18) is applied at all cell surfaces. Note that due to the elliptic character of the equation, the flow variables at the surfaces are taken as the arithmetic averages of the cell-centered values. Also note that all the metrics are computed at cell surfaces. After substituting the surface current density into the discretized current continuity equation (16), we obtain our 19-point stencil. The stencil takes account of more points than the standard central-difference scheme that includes only seven points and is accurate for orthogonal grids. The extra points in our stencil are necessary to evaluate the metrics and variable derivatives. The mathematical details are trivial and neglected here.

## IV. Solution Strategy for the Poisson Equation

The relaxation method is based on the approximate factorization (AF) method in [4,9]. For the 19-point stencil, the AF scheme can be written as

$$(\alpha_p + a_{1i-1} + b_{1i} + c_{1i+1})\Delta\phi^{(1)} = \alpha_p^2 R \tag{27}$$

$$(\alpha_p + a_{2j-1} + b_{2j} + c_{2j+1})\Delta\phi^{(2)} = \Delta\phi^{(1)} \tag{28}$$

$$(\alpha_p + a_{3k-1} + b_{3k} + c_{3k+1})\Delta\phi = \Delta\phi^{(2)} \tag{29}$$

where $R$ is the residual, for which the expression is taken directly from the 19-point stencil and neglected here, and $\alpha_p$ is the relaxation

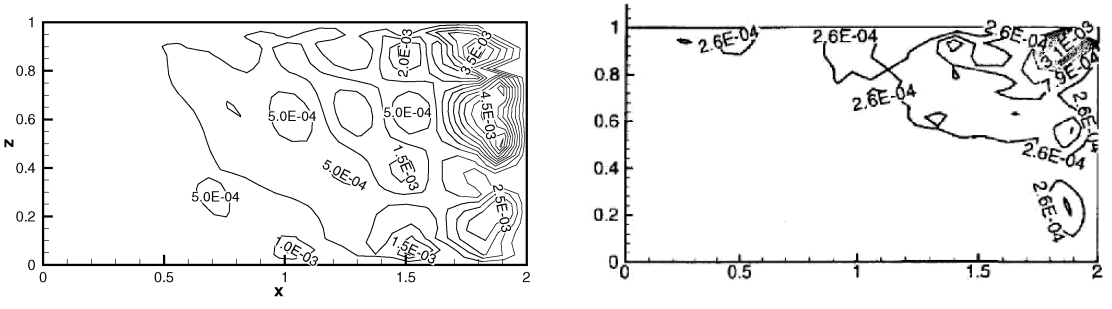


a) b)

**Fig. 3 Error of the computed result compared with theoretical solution: a) present result and b) result from [4].**

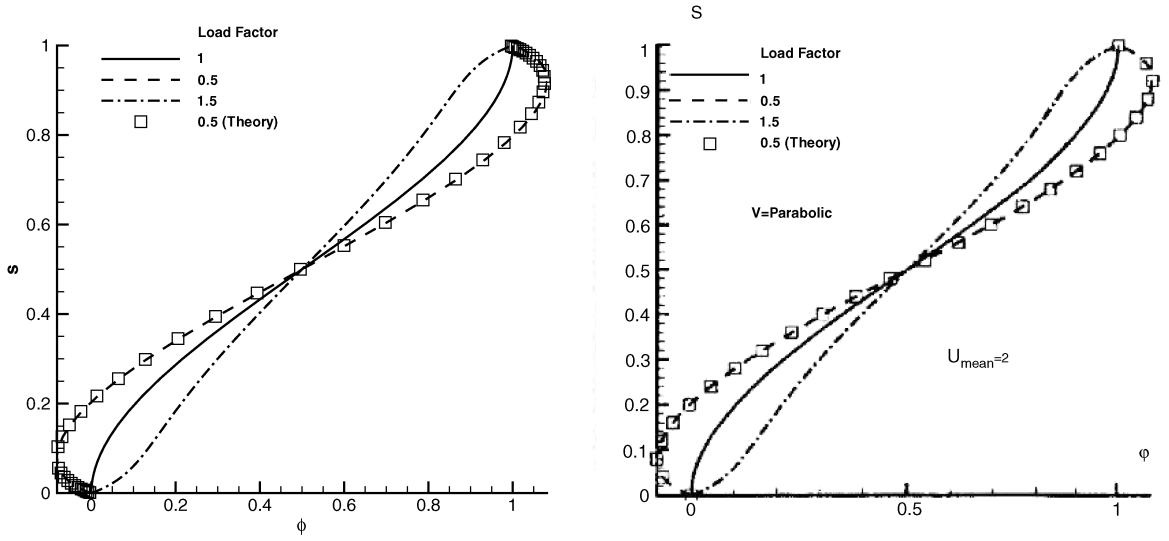


a) b)

**Fig. 4 Potential distribution at load factors 0.5, 1, and 1.5 for the inclined-electrodes case: a) present result and b) result from [4].**

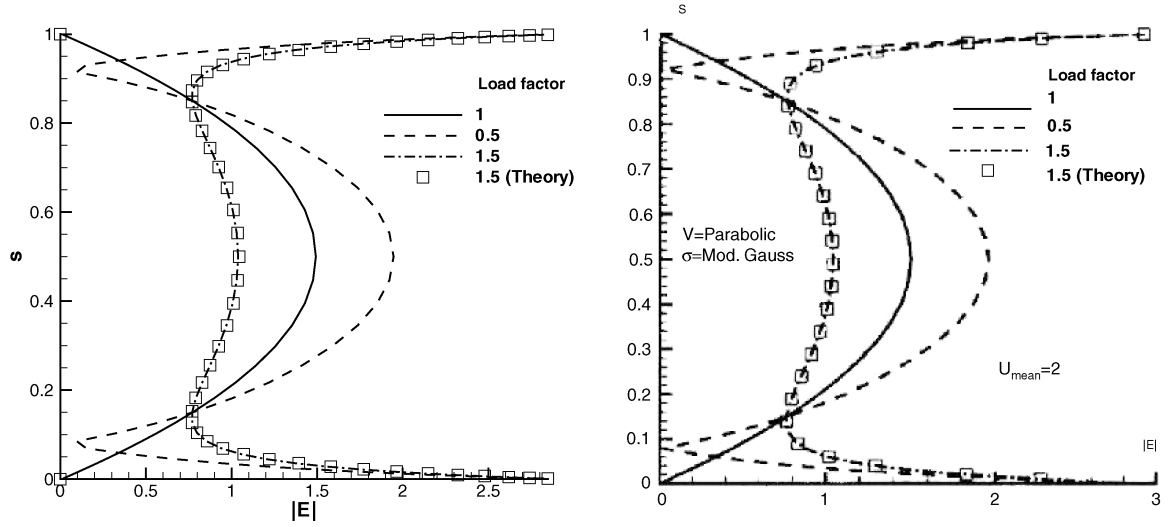


a) b)

**Fig. 5 Electric field at load factors 0.5, 1, and 1.5 for the inclined-electrodes case: a) present result and b) result from [4].**

parameter of typical value between 0.01 and 0.001. The coefficients $a_i$, $b_i$, and $c_i$ are, for example,

$$a_{1i-1} = -\bar{\xi}_{i-1/2} - \tfrac{1}{4}(-\bar{\xi}_{j+1/2} + \bar{\xi}_{j-1/2} - \bar{\xi}_{k+1/2} + \bar{\xi}_{k-1/2}) \quad (30)$$

$$b_{1i} = \bar{\xi}_{i+1/2} + \bar{\xi}_{i-1/2} \quad (31)$$

$$c_{1i+1} = -\bar{\xi}_{i+1/2} + \tfrac{1}{4}(-\bar{\xi}_{j+1/2} + \bar{\xi}_{j-1/2} - \bar{\xi}_{k+1/2} + \bar{\xi}_{k-1/2}) \quad (32)$$

and $a_2$, $b_2$, and $c_2$ and $a_3$, $b_3$, and $c_3$ can be found similarly.

When this method is applied to the regimes of interest in this paper, poor performance is obtained due to some special features of our cases. First, there is a strong shock present, which introduces strong gradients of the variables. If small $\alpha_p$ is used, the computation becomes unstable. Second, a parallel version of the AF method is needed, due to the large size of the grid ($\sim 10^6$ grid points) used. Finally, the topology of our cases, in which two electrodes exist

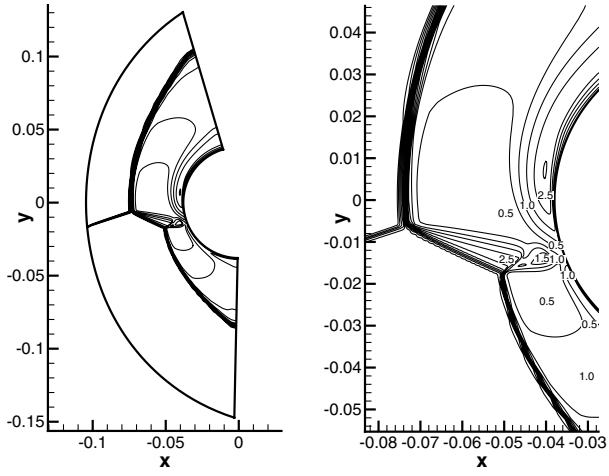


**Fig. 6 Mach number contours of the type IV shock–shock interaction case.**

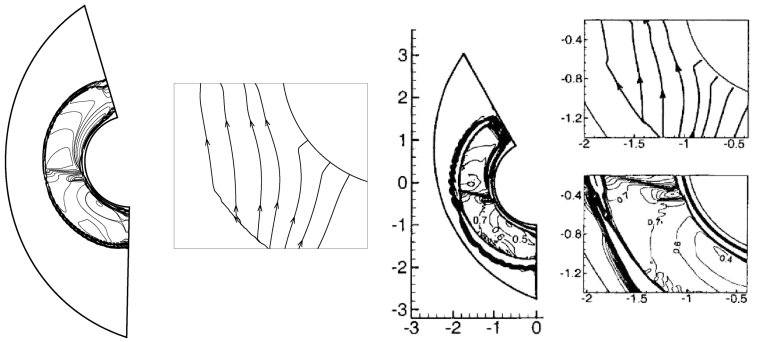

a) b)

**Fig. 7 Electric field distribution of the type IV shock–shock interaction case: a) present result and b) result from [4].**

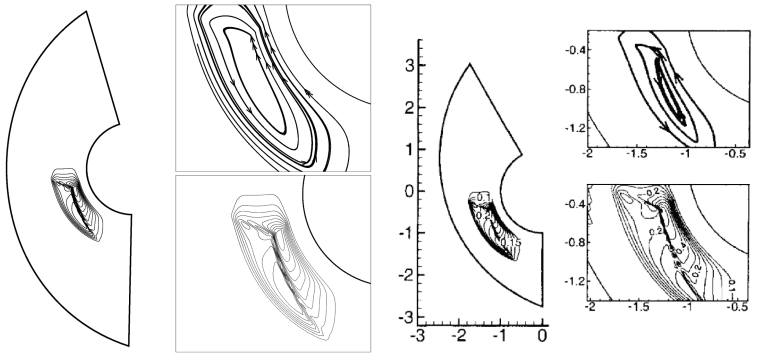

a) b)

**Fig. 8 Current distribution of the type IV shock–shock interaction case: a) present result and b) result from [4].**

inside the computational domain, requires additional modifications to the line-relaxation sweeps.

We apply the DPLR [6] algorithm and modify the AF method, which results in a method written as

$$(\alpha_p + a_{3k-1} + b_{3k} + c_{3k+1})\Delta\phi^{(1)} = \alpha_p R \tag{33}$$

$$(\alpha_p + a_{2j-1} + b_{2j} + b_{1i} + c_{2j+1})\Delta\phi^{(2)} = \Delta\phi^{(1)} \tag{34}$$

1) Do $n = 3$,

$$n_{\max} + 3(\alpha_p + a_{2j-1} + b_{2j} + b_{1i} + c_{2j+1})\Delta\phi^{(n)} = \Delta\phi^{*} - a_{1i-1}\Delta\phi_{i-1}^{(n-1)} - c_{1i+1}\Delta\phi_{i+1}^{(n-1)}$$

2) End do

$$\Delta\phi = \Delta\phi^{(n_{\max}+3)}$$

In practice, we use $n_{\max} = 4$.

Figure 2 plots the residual versus iteration step. As seen in the figure, the modified AF with DPLR has a faster convergence rate than the original AF. However, for fully coupled simulations with the MHD flow solver, the convergence rate is still not satisfactory, and we are investigating alternative solution approaches [10,11].

## V. Code Validation

All the test cases in this section are taken from [4]. The use of the figures from the reference is with permission. The first test is to compare the result of the code to an analytic solution. The governing equation of the test problem is

$$\frac{\partial^2\phi}{\partial x^2} + \frac{\partial^2\phi}{\partial z^2} = xe^z \tag{35}$$

on the domain $0 \le x \le 2,\ 0 \le z \le 1$ subject to the Dirichlet boundary conditions:

$$\phi(x=0,z) = 0, \qquad \phi(x=2,z) = 2e^z$$
$$\phi(x,z=0) = x, \qquad \phi(x,z=1) = xe \tag{36}$$

The theoretical solution of the test problem is $\phi = xe^z$. The grid used has $51 \times 26 \times 3$ points which follows the wavy pattern of the grid in [4], which has $51 \times 26 \times 7$ points. Figure 3 plots the error that is the difference between computational and theoretical solutions. As seen in Fig. 3, the computational error is below 0.45%.

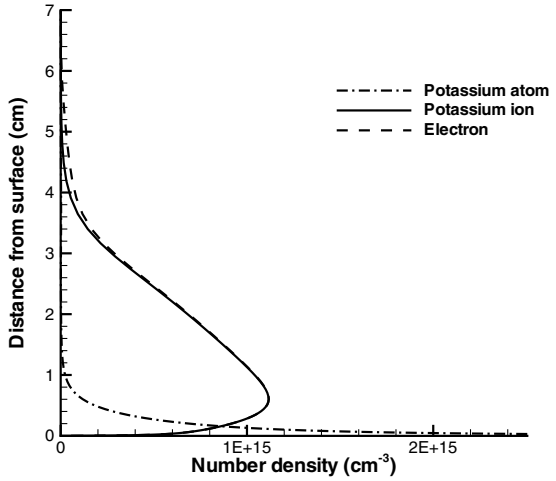


**Fig. 9 Number densities of $K$, $K^+$, and $e^-$ in the boundary layer at $x = 0.8$ m.**

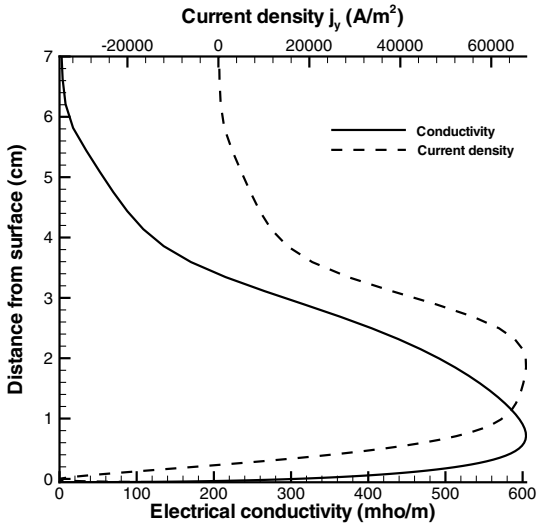


**Fig. 10 Electrical conductivity and current density in the boundary layer at $x = 0.8$ m.**

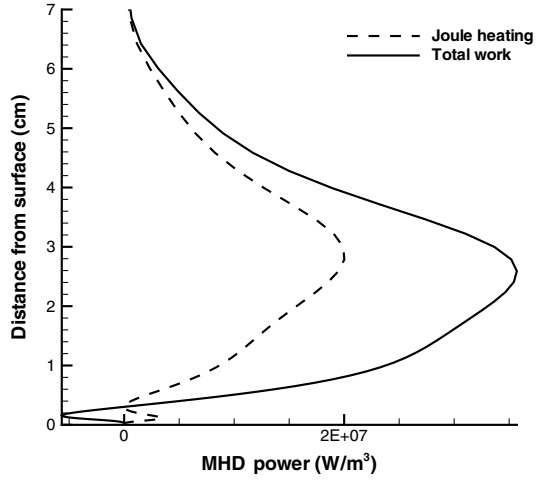


**Fig. 11 Joule heating and rate of the total MHD work per cubic meter in the boundary layer at $x = 0.8$ m.**

The second test case is about two inclined electrodes separated by a distance $S = 1$. The computational grid follows the same wavy pattern in [4]. Two electrodes are assigned potentials 0 and 1, and the conductivity distribution is specified by a modified Gaussian function:

$$\sigma(r - r_0) = Ce^{-a(r-r_0)^6} \tag{37}$$

where $r_0$ is the center of the distribution, $C$ is set to unity, and

$$a = \frac{1}{\delta^6}\ln\left(\frac{C}{\epsilon}\right) \tag{38}$$

The velocity profile and theoretical solutions can be found in [4]. Different values of magnetic field are chosen to set the load factors

**Table 1 Boundary conditions for the Poisson solver**

| Direction | Boundary |
|---|---|
| $\xi_{\min}$ (stagnation plane) | Plane of symmetry |
| $\xi_{\max}$ (outflow) | $d\phi/d\xi = 0$ |
| $\eta_{\min}$ (vehicle surface) | Dielectric wall $\Leftrightarrow j_{\text{wall}} = 0$ |
| $\eta_{\max}$ | Far field |
| $\zeta_{\min}$ and $\zeta_{\max}$ | Periodic |

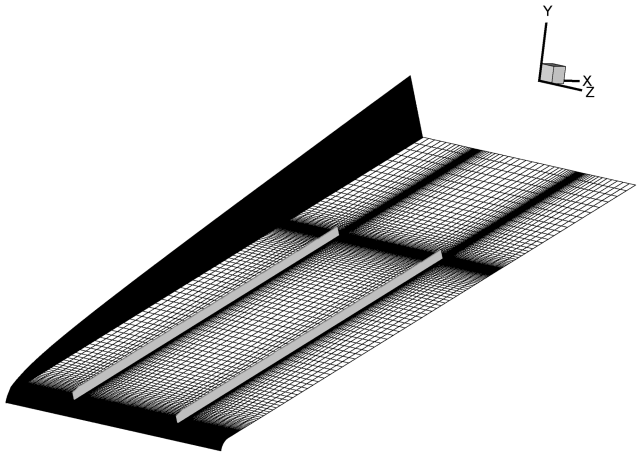


**Fig. 12 The 200 × 100 × 102 grid for the 4 m model.**

0.5, 1, and 1.5. Figures 4 and 5 plot the computed potential and electric field distributions between the electrodes, and they show that our results reproduce the theoretical solution and the results in [4].

The type IV shock–shock interaction is taken as our last test case. We use a grid of size $456 \times 101 \times 3$, compared with that of $101 \times 101 \times 7$ in the reference. The flow conditions can be found in [4]. Figure 6 plots the Mach number contours that are computed by our MHD flow solver. To be consistent with the referenced paper, the initial electromagnetic effect is shown and the MHD effects in the flow solver are turned off. The imposed conductivity distribution is taken from [4], which has the maximum value at a distance of 0.5 radii away from the cylinder surface and $\theta = -10$ deg. Figures 7 and 8 show the electric field and current distributions compared with the reference. Note that our result does not incur oscillation across the discontinuity, and the resolution of our result is somewhat lower. This is because in the referenced paper, a scheme of up to sixth order is used that introduces oscillations near discontinuities; whereas a second-order scheme is used in the present work, and no oscillation is observed in the results. Despite that, all of our results reproduce those in the reference.

## VI. Results for an MHD Generator Onboard a Reentry Vehicle

This section presents the results on MHD power generation onboard a reentry vehicle. The inflow condition for the flow solver is set at a 46 km altitude ($\rho_\infty = 1.7141 \times 10^{-3}$ kg/m$^3$ and $T_\infty =$ 266.93 K). The inflow velocity and Mach number are 7000 m/s and 21.37, respectively. Thus, with 1% seeding, the mass flow of seed is 3.6 g/s per meter width of the vehicle. The temperature at the vehicle surface is set constant at 1000 K.

The imposed magnetic induction distribution is assumed to be uniform:

$$B(y) = 0.2 \text{ T} \tag{39}$$

The direction of the magnetic induction vector is perpendicular to the vehicle surface.

Figure 9 reproduces the previous result of number densities of $K$, $K^+$, and $e^-$ along the $x = 0.8$ m line. The $x = 0.8$ m line is perpendicular to the vehicle surface and of 0.8 m axial distance downstream from the vehicle nose. It shows that the density of electrons reaches to $10^{15}$ cm$^{-3}$ in the boundary layer, and closer to the vehicle wall, the potassium ions and electrons recombine. Even though the wall boundary condition is noncatalytic, our high-resolution grid in the boundary layer captures the recombination reactions near the wall. Figure 10 plots the conductivity and current density along the line $x = 0.8$ m. Their maximum values occur at about 1 or 2 cm away from the wall and then drop rapidly even closer to the wall. Note that the conductivity is theoretical without considering the mixing efficiency of the seed with flow.

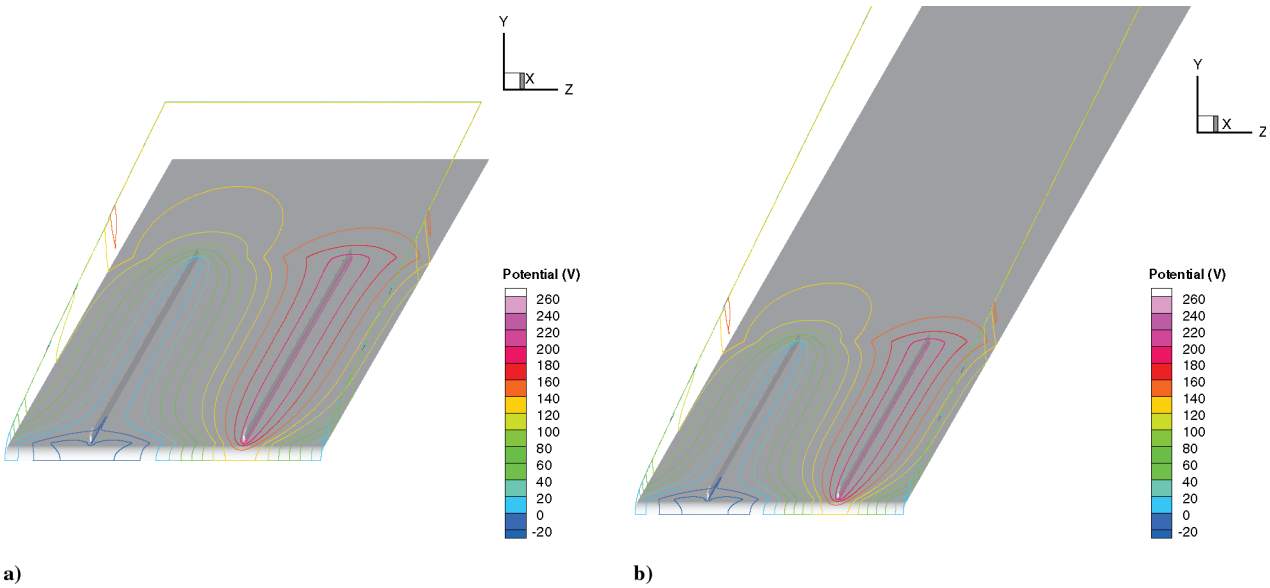


**Fig. 13 Electric potential contours of the 4 and 8 m models.**

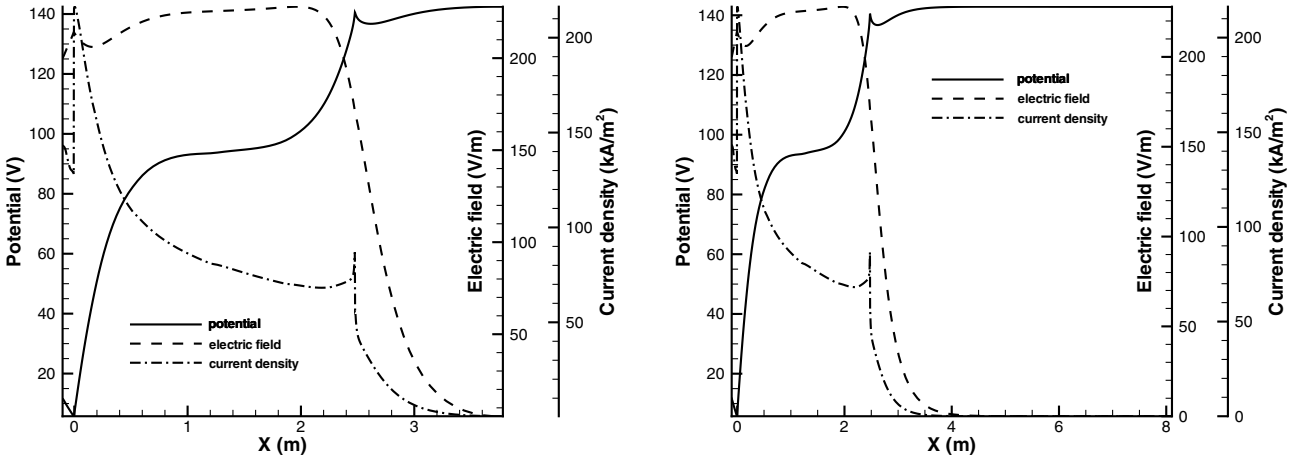


**Fig. 14 Variations of potential, electric field and current density along the line on the center plane between the two electrodes and 3 cm above the vehicle surface: a) 4 m model and b) 8 m model.**

The load factor is set at 0.5 to maximize the power extraction. The total work done by the MHD devices has the effect of slowing down the flow and converts the flow kinetic energy into electrical and internal energy. For a load factor of 0.5, either Joule heating or power extraction equals one-half of rate of the total MHD work. Figure 11 plots Joule heating and rate of the total work per cubic meter along the line $x = 0.8$ m.

The boundary conditions for the Poisson solver are shown in Table 1 (the $\xi$, $\eta$, and $\zeta$ directions are associated with the streamwise, vehicle body normal, and spanwise directions, respectively). We make two notes about the boundary conditions:

1) The periodic boundary condition in the $\zeta$ direction is from the assumption that there is an array of electrodes arranged periodically in the spanwise direction.

2) The outflow boundary condition $d\phi/d\xi = 0$ assumes that the outflow boundary has been extended far enough that the potential variation is small.

To examine how far away the outflow boundary should be positioned, we compare two vehicle models, with 8 and 4 m lengths, respectively. For the 8 m model, a grid of 250 by 100 by 102 points in the $\xi$, $\eta$, and $\zeta$ directions, respectively, is used. For the 4 m model, a 200 by 100 by 102 grid is used. Figure 12 shows the grid for the 4 m model. Cathode and anode potentials are 0 and 221.28 V, which is an output of our MHD flow solver using a load factor of 0.5 [3]; that is, the MHD flow solver computes the distribution of the electromotive force (emf) between the electrodes and assigns the potential difference to be one-half of the space-averaged emf value.

Figure 13 plots the computed potential contours for the 4 and 8 m models. Figure 14 plots the potential, electric field, and current variation along the line on the center plane between the two electrodes and 3 cm above the vehicle surface. The results show that in the region beyond 4 m, the potential reaches a uniform distribution, which results in negligible current density and electric field. Therefore, the 4 m outflow boundary is extended far enough for this case.

Because we use a finite volume method, the current conservation condition is automatically satisfied. Hence, the net current crossing

**Table 2 Computed current at boundaries**

| Direction | Current, A |
|---|---|
| $\xi_{\min}$ | $-4.6 \times 10^{-4}$ |
| $\xi_{\max}$ | $5.1 \times 10^{-4}$ |
| $\eta_{\min}$ | 0 |
| $\eta_{\max}$ | 0 |
| $\zeta_{\min}$ | −4374.9 |
| $\zeta_{\max}$ | 4374.9 |

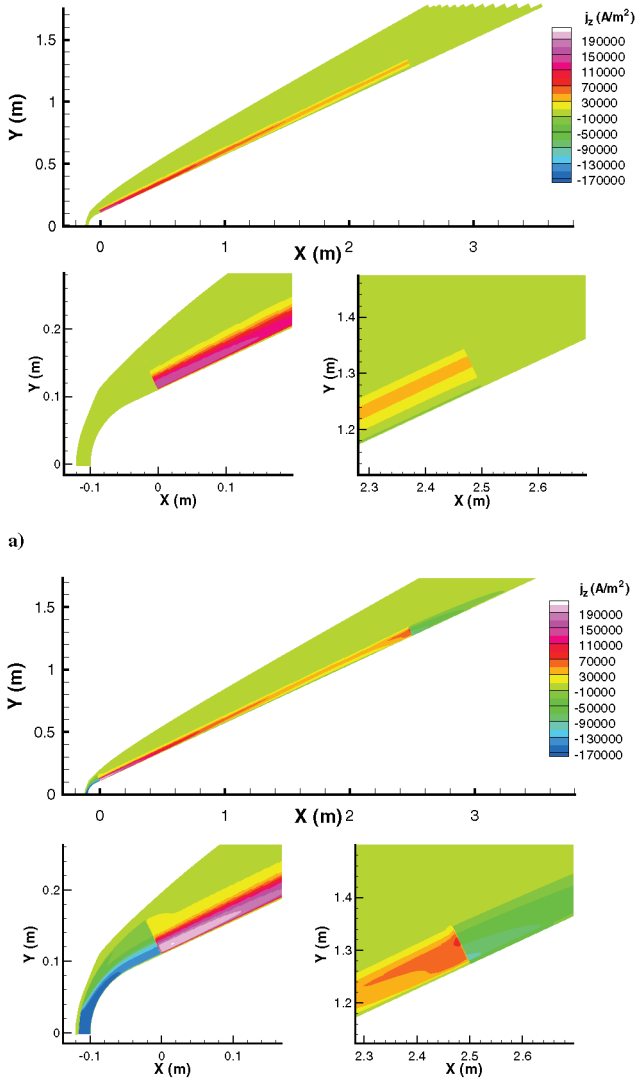


**Fig. 15 Contours of the $z$-direction current density at 1% NaK seed: a) previous 2-D result and b) 3-D Poisson solver result. The plot is at the midplane ($z = 0$) between the electrodes.**

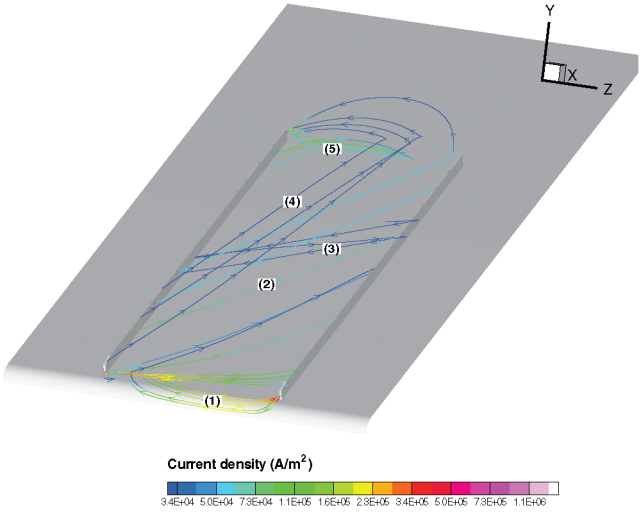


**Fig. 16 Current-density stream traces. The current is in the tangential direction to the line, and the color contours show the magnitude of the current density.**

the boundaries of the computational domain should be zero. Also, except for the two periodic boundaries in the $\zeta$ direction, the total current across every boundary should be zero. The computed current at the boundaries is shown in Table 2.

Although the previous simulations [1–3] assume uniform distributions of the electric parameters in the $\zeta$ direction, the present model takes into account three-dimensional variations of the electric field and current density. Figure 15 plots the $z$-direction (spanwise) current-density contours from the previous and present 3-D calculations. For comparison purposes, the current density from the 3-D modeling is plotted at the center plane between the electrodes. Although both results show a pattern similar to the current distribution, the 2-D result neglects the current which travels in front of the inlet and behind the outlet. Also, the current density is underpredicted by the 2-D simulation near the inlet and outlet.

Figure 16 plots the current-density stream traces. From the nose to the base of the vehicle, there are five types of current, which we refer to as the 1) anode current eddy, 2) cross electrode current, 3) boundary-layer current, 4) top current, and 5) cathode current eddy. The extracted current is mostly due to the cross electrode current, type 2, which leaves the cathode and enters the anode. This current flows at several centimeters away from the surface, where both conductivity and emf are high. Closer to the vehicle surface, where the emf $\mathbf{u} \times \mathbf{B}$ is low, the electric field directed opposite to the emf dominates. Hence, there exists current from the anode to the cathode in the boundary layer, which we refer to as type 3. Figure 17

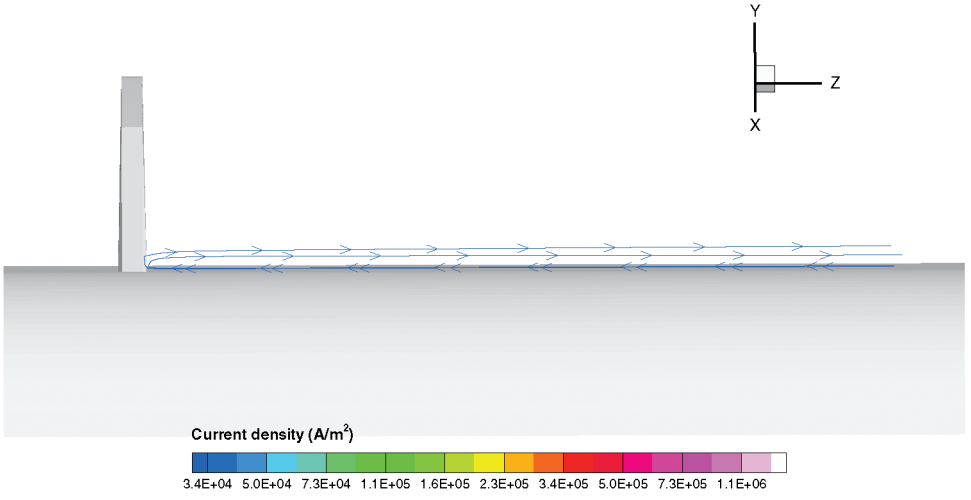


**Fig. 17 Current circulation in the boundary layer.**

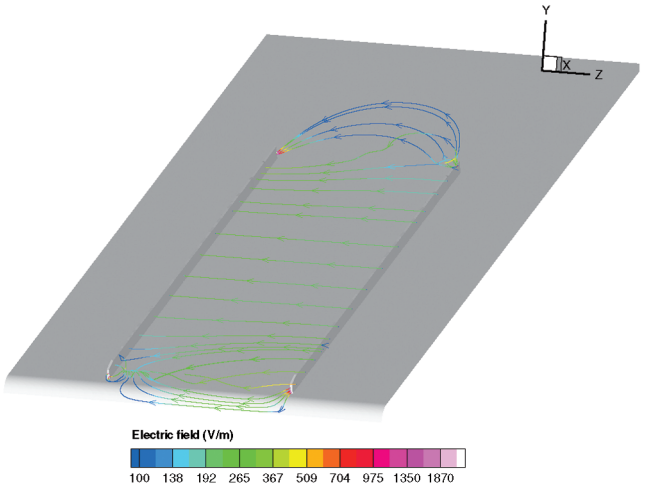


**Fig. 18 Electric field stream traces. The electric field is in the tangential direction to the line, and the color contours show the magnitude of the electric field.**

shows that there is current circulation near the vehicle surface, which is formed by types 2 and 3 currents. There is also current going across the electrodes from the top edges, which is a small value because the conductivity is small above 7 cm away from vehicle surface. The averaged Hall parameter is about 1.2, and the current lines are obviously inclined.

Figure 18 plots the electric field stream traces, for which the direction and color show the direction and magnitude of the electric field. It shows that the electric field is strong near the upstream end of the anode and the downstream end of the cathode. Although the electric field is distorted in the region near the inlet and outlet, it exhibits a uniform distribution in most of the region between the electrodes.

The previously computed power extraction [1–3] is 1.249 MW for 1% seeding, assuming uniform electric field and two-dimensional current distributions. With the present model, the total current that goes through one pair of electrodes is 4.392 kA, and the corresponding power extraction is 0.972 MW. Table 3 lists the total current on each electrode surface (positive is defined as leaving the electrodes, and negative is defined as entering the electrodes). The power lost is due to anode and cathode current eddies that were not computed by the previous model.

## VII. Conclusions

In the present work, a numerical tool was developed to solve the Poisson equation for the electric potential distribution around a reentry vehicle with onboard electrodes and magnets. A 19-point-stencil finite volume method was used and the discretized form of the Poisson equation was presented. We solved the equation with a modified parallel approximate factorization (AF) method, which showed better performance than the basic AF. The tool was tested with three cases, and all the results reproduced analytic solutions and previous numerical results.

We then applied the Poisson solver to MHD power-generation cases. The computed current and electric field patterns were shown, which are three-dimensional and have the highest magnitude at the upstream side of the anode and the downstream side of the cathode. From the figure, we categorized the current into five types, of which type 2 contributes the most to the extracted power. The computed power extraction is found to be 22% less than the previous 2-D result, because of both three-dimensional effects of the current and slightly narrower spacing between the electrodes.

For future work, faster convergence of the Poisson solver would be required for running more cases in a much faster way. The Poisson solver and the MHD flow solver should be fully coupled and used to calculate the boundary-layer and near-electrode sheath regions. More realistic seed injection, electrode shape, and magnetic field profiles would have to replace the present approximate model. For example, one can simulate injection through vehicle surface, flush electrodes, and magnetic dipoles in the future.

## Acknowledgments

This material is based upon work supported by the U.S. Air Force Office of Scientific Research (AFOSR) Unsteady Aerodynamics and Hypersonics Research Program under contract FA9550-04-C-0121. A portion of this work was also sponsored by the AFOSR under grant FA9550-04-1-0341. The views and conclusions contained herein are those of the author and should not be interpreted as necessarily representing the official policies or endorsements, either expressed or implied, of the AFOSR or the U.S. Government.

## References

[1] Macheret, S. O., Shneider, M. N., and Candler, G. V., "Modeling of MHD Power Generation on Board Reentry Vehicles," AIAA Paper 2004-1024, Jan. 2004.

[2] Macheret, S. O., Shneider, M. N., Candler, G. V., Moses, R. W., and Kline, J. F., "Magnetohydrodynamic Power Generation for Planetary Entry Vehicles," AIAA Paper 2004-2560, June 2004.

[3] Wan, T., Candler, G. V., Macheret, S. O., Shneider, M. N., and Miles, R. B., "CFD Modeling and Simulations of MHD Power Generation During Re-Entry," AIAA Paper 2004-2562, June 2004.

[4] Gaitonde, D. V., and Poggie, J., "Elements of a Numerical Procedure for 3-D MGD Flow Control Analysis," AIAA Paper 2002-0198, Jan. 2002.

[5] Visbal, M. R., and Gaitonde, D. V., "Computation of Aeroacoustic Fields on General Geometries Using Compact Differencing and Filtering Schemes," AIAA Paper 99-3706, 1999.

[6] Wright, M. J., Bose, D., and Candler, G. V., "Data-Parallel Line Relaxation Method for the Navier–Stokes Equations," *AIAA Journal*, Vol. 36, No. 9, 1998, pp. 1603–1609. doi:10.2514/2.586

[7] Candler, G. V., "The Computation of Weakly Ionized Hypersonic Flows in Thermochemical Nonequilibrium," Ph.D. Thesis, Stanford Univ., Stanford, CA, 1988.

[8] Sutton, G. W., and Sherman, A., *Engineering Magnetohydrodynamics*, McGraw–Hill, New York, 1965.

[9] Holst, T. L., "Transonic Flow Computations Using Nonlinear Potential Methods," *Progress in Aerospace Sciences*, Vol. 36, No. 1, 2000, pp. 1–61. doi:10.1016/S0376-0421(99)00010-X

[10] "HYPRE User's Manual," Center for Applied Scientific Computing, Lawrence Livermore National Lab., Livermore, CA, July 2001.

[11] Schaffer, S., "A Semi-Coarsening Multigrid Method for Elliptic Partial Differential Equations With Highly Discontinuous and Anisotropic Coefficients," *SIAM Journal on Scientific Computing*, Vol. 20, No. 1, 1998, pp. 228–242. doi:10.1137/S1064827595281587

K. Powell
*Associate Editor*